Reduced Graphene Oxide decorated with Manganese Cobalt Oxide as Multifunctional Material for Mechanically Rechargeable and Hybrid Zinc-Air Batteries

Qaseem, Adnan; Chen, Fuyi; Qiu, Chuanzhou; Mahmoudi, Abdelaziz; Wu, Xiaoqiang; Wang, Xiaolu; Johnston, Roy L.

DOI:
10.1002/ppsc.201700097

WILEY-VCH

DOI: 10.1002/ ((please add manuscript number))
Article type: Full Paper

Manganese Cobalt Oxide Decorated Reduced Graphene Oxide as Multifunctional Material for Mechanically Rechargeable and Hybrid Zinc Air Batteries

Adnan Qaseem , Fuyi Chen, Chuanzhou Qiu, Abdelaziz Mahmoudi, Xiaoqiang Wu , Xiaolu Wang and Roy L. Johnston**

Adnan Qaseem, Prof. Fuyi Chen, Chuanzhou Qiu, Abdelaziz mahmoudi, Xiaoqiang Wu and Xiaolu Wang
State Key Laboratory of Solidification Processing, Northwestern Polytechnical University, Xian, 710072, China
E-mail: fuyichen@nwpu.edu.cn

Prof. Roy L. Johnston
School of Chemistry, University of Birmingham, Birmingham, B15 2TT, U.K.
E-mail: r.l.johnston@bham.ac.uk

Keywords: bifunctional catalyst, hydrothermal synthesis, primary zinc-air battery, hybrid zinc-air battery, energy conversion and storage.

Spinel $MnCo_2O_4$ nanoparticles on nitrogen doped reduced graphene oxide ($MnCo_2O_4$/NGr) are synthesized for advanced zinc air batteries with remarkable cyclic efficiency and stability. The synthesized $MnCo_2O_4$/NGr exhibits ORR activity with a half-wave potential $E_{1/2}$ of 0.85 V (vs. RHE), comparable to the commercial Pt/C with $E_{1/2}$ of 0.88 V (vs. RHE) along with superior oxygen electrode activity ΔE = 0.91 V for ORR/OER in alkaline media. Short and long term durability tests show that $MnCo_2O_4$/NGr is more stable than Pt/C in alkaline environment. When deployed in a mechanically rechargeable zinc-air system, the $MnCo_2O_4$/NGr functions with a stable discharge profile of 1.2 V at 20 $mA.cm^{-2}$, a large discharge capacity of 707 $mAh.g^{-1}_{Zn}$ at 40 $mA.cm^{-2}$ and a high energy density of 813 $Wh.Kg^{-1}_{Zn}$ under ambient air. Electrically rechargeable $MnCo_2O_4$/NGr zinc-air battery displays hybrid behavior with both faradaic and oxygen redox charge-discharge characteristics, operating at higher voltage and providing higher power density and excellent cyclic efficiency of 86% for over 100 cycles compared to Pt/C with efficiency of around 60%. Hybrid zinc air

battery operates with a stable and energy efficient profile with low charge-discharge gap at current densities of 1, 5 and 10 mA.cm^{-2}.

1. Introduction

The harmful effects of fossil fuel based energy systems on the environment along with their sustainability concerns have provided the impetus for research on advanced energy conversion and storage systems. Multifunctional energy storage materials and devices are a subject of great interest as they can meet the global demand of clean and sustainable energy.[1] Metal-air batteries (M= Li, Zn, Al etc.) are the epitomes of these systems with the Li-air battery having the highest energy density.[2] Although Li-air battery has the highest theoretical energy density, the commercialization of Li-air system faces numerous safety and stability issues due to highly reactive nature of lithium.[3] Zn-air battery is especially attractive for commercialization point of view because of its high energy density, non-toxicity and abundance of Zn in the earth's crust.[4] The theoretical energy density of Zn-air battery is about 4 times higher than the Li-ion battery. The commercialization of secondary Zn-air battery is impeded because of high catalyst cost, poor stability and low power density along with issues such as dendrite formation during recharge cycle, formation of ZnO on anode and electrolyte leakage.[5] The mechanically rechargeable system alleviates the issue of Zn-dendrite formation by simple replacement of the Zn anode after each discharge cycle. By continuously replacing the metallic anode after each discharge, the Zn-air battery is stable for operation repeatedly. However, mechanical rechargeable systems also faces issues like i) high cost of expensive commercial Pt/catalyst used for ORR along with ii) poor durability owing to the instability of Pt/C over period of time in alkaline media which leads to gradual decay of the battery performance.[6]

Transition metal oxides decorated on carbon nanomaterials have been reported as bifunctional electrocatalysts in alkaline environment.[7] The strategy of introducing metal oxide nanoparticles (NPs) onto conductive carbon framework alleviates the problem of poor

conductivity which is associated with most of metal oxide NPs due to their low d-band mobility.[8] Oxides of cobalt are of especial interest because of their inherent high OER activity. In Co_3O_4, the mix valence of Co^{+2} and Co^{+3} in the spinel structure is reported to play a vital role during ORR.[9] A further improvement towards catalytic activity in the cobalt oxide spinel is reported by the introduction of mix valence states of Mn^{+3} and Mn^{+4} into the structure by doping with manganese. The introduction of manganese improves the M-O-C and M-N-C bonding along with an increase in the catalytically active surface area.[10] Liang *et al.* developed manganese-cobalt oxides on N-doped reduced graphene oxide ($MnCo_2O_4$/N-rmGO) for ORR in alkaline media by solvothermal treatment of metallic salts with ammonia solution in ethanol.[10] The $MnCo_2O_4$/N-rmGO was reported to have a better catalytic activity for ORR than Co_3O_4/N-rmGO hybrid but the OER activity of $MnCo_2O_4$/N-rmGO was found to be lower than the Co_3O_4/N-rmGO. Porous spinel microspheres of cobalt and manganese mixed oxides ($CoMn_2O_4$/C and Co_2MnO_4/C) as highly efficient multifunctional catalysts were prepared by the thermal degradation of the respective carbonate precursors at 400 ^oC.[11] Tetragonal $CoMn_2O_4$/C catalyst was observed to be more active for ORR whereas cubic $MnCo_2O_4$/C was more active for OER, however, the half-wave potential $E_{1/2}$ of $CoMn_2O_4$/C was 90 mV lower than that of the commercial Pt/C catalyst. Similarly $CoMn_2O_4$ anchored onto nitrogen doped reduced graphene (N-rGO) oxide was reported by hydrothermal method for Zn-air battery.[12] The half-wave potential $E_{1/2}$ of $CoMn_2O_4$/N-rGO was 50 mV more positive compared to $CoMn_2O_4$/rGO and 60 mV more negative compared to the commercial Pt/C, respectively. Also, nickel cobalt oxide supported on reduced graphene oxide nanosheets $NiCo_2O_4$-rGO hybrid was reported by a facile chemical route with catalytic activity comparable to commercial Pt/C in terms of onset potential and current density.[13] To further improve the oxygen reduction property of the $MnCo_2O_4$/NGr, one way is to embed the oxides or metal into graphene, another is to make the oxides or metal to form the nanoporous structures.[14] More recently, hybrid zinc air batteries employing transition metal oxide

faradaic transitions have been reported to the improve power density and stability of zinc air battery. By growing $NiCo_2O_4$ nanowires onto carbon coated Ni-foam, a hybrid zinc air battery with high working voltage and high power density has been reported.[15] The faradaic redox transitions i.e. M-O↔M-O-OH of M=Ni,Co induce hybrid charge-discharge behavior enabling the battery to work at a higher voltage with high power density. Similarly a hybrid zinc air battery with high power density and energy density was reported using $NiO/Ni(OH)_2$ as the active material.[16] The combination of faradaic redox reactions of the active nickel species along with conventional ORR/OER at cell level was ascribed as the reason behind the high energy density and power density of the hybrid battery.

Herein, we synthesize $MnCo_2O_4$ nanoparticles anchored onto nitrogen doped reduced graphene oxide ($MnCo_2O_4$/NGr) by hydrothermal treatment and explore their electrocatalytic activity for ORR/OER in alkaline media along with supercapacitive properties. Primary and mechanically rechargeable Zn-air batteries were made to confirm the activity and stability for ORR in a practical application. The batteries were observed to function with an activity similar to commercial Pt/C along with much superior stability in ambient air. A negligible loss in discharge potential was observed after several recharges in the mechanical rechargeable Zn-air battery. $MnCo_2O_4$/NGr electrocatalyst was also observed to be active for OER. The ΔE value for the $MnCo_2O_4$/NGr system was recorded to be 0.91 V which also confirms its superior bifunctional (ORR/OER) activity. Hybrid zinc air battery data reveals that the combination of supercapacitive and ORR/OER reactions enables the battery to function at higher discharge voltage resulting in high power density, exceptional cyclic efficiency and low charge-discharge potential gap at current densities of 1, 5 and 10 $mA.cm^{-2}$.

2. Results and Discussion

Figure 1 shows the XRD patterns of the as synthesized catalysts. Complete formation of spinel $MnCo_2O_4$ on graphene is confirmed by the presence of well-defined peaks at 2θ values of 30.6°, 36.1° , 43.9 ° , 58.2 ° and 63.6 ° corresponding to the (220), (311), (400), (511)

and (440) planes respectively according to the JCPDS PDF card # 23-1237. The peak present in all the patterns at about 2θ value of 25° corresponds to the reduced graphene support used for the decoration of metal oxide nanoparticles. In case of use of only cobalt acetate salt during hydrothermal treatment, most of the precursor is converted to spinel Co_3O_4 as confirmed by the peaks located at 31° , 36.8 °, 59.3 ° and 65.2 ° which are ascribed to (220), (311), (511) and (440) planes respectively. However apart from Co_3O_4,diffraction peak from cobalt hydroxide is also present which shows that during the hydrothermal synthesis mixture of cobalt oxide/hydroxide have been formed on the surface of graphene. This is in agreement with the hydrothermal synthesis of different cobalt oxides by Dong *et al.* which also report a degree of different oxide formation from cobalt acetate during the hydrothermal process.[17] In case of Manganese acetate precursor, formation of spinel Mn_3O_4 on graphene was confirmed with the presence of several Mn_3O_4 peaks attributed to JCPDS PDF card # 24-0734.

The SEM of a graphene flake decorated with $MnCo_2O_4$ is shown as **Figure 2**a. Plenty of $MnCo_2O_4$ nanoparticles are observed to be uniformly distributed on the graphene flakes. The atomic ratio of Mn:Co was also estimated and found to be nearly 1:2 over a point (spectrum 1) and a region (spectrum 2) as shown in Figure S1 in Supporting Information. The atomic ratio of Mn:Co is consistent with the molar ratios of metallic salt precursors i.e. 1:2 used for the formation of spinel $MnCo_2O_4$. Apart from the elements of spinel metal oxide, a few peaks from the glass substrate used for SEM are also present at 1.75 and 3.5 keV respectively. Figure 2 (b, c) show low magnification TEM of $MnCo_2O_4$/NGr along with selected area electron diffraction (SAED). The crystallinity of the sample is confirmed by the presence of discernable rings. These rings are related to the diffraction of electrons from (220), (311), (400), (511) and (440) planes of $MnCo_2O_4$. The SAED data is in agreement with the XRD results which also show formation of pure $MnCo_2O_4$ on graphene flakes with the absence of impurities. The high density of (311) facets of $MnCo_2O_4$ in HRTEM is in consistency with the XRD data which show a preferential diffraction from the (311) planes with interplanar

spacing value of 0.25 nm (Figure 2d). Also lattice fringes from (400) with d=0.21 nm are also visible in HRTEM. Moreover the dispersion of $MnCo_2O_4$ nanoparticles is uniform and homogeneous on graphene sheets on both macro and micro levels as evident from the SEM and TEM (Figure S2 in Supporting Information). Elemental mapping of the sample reveals a uniform dispersion of constituent elements across the area of interest. The treatment of the GO with ammonia reduces the GO to reduced graphene oxide along with its nitrogenation as confirmed by presence of nitrogen in Figure S2. These N doped sites in graphene are reported to be the anchoring sites for the nucleation and growth of nanoparticles. The uniform incorporation of N into the graphene sheets is therefore pivotal for the subsequent uniform dispersion of the metal oxide nanoparticles.[9] Moreover to look into the effect of morphology on the electrocatalytic performance, we also carried out SEM and TEM analysis on the reference samples (Figure S3 in Supporting Information). The uniform dispersion of both Co_xO_y and Mn_3O_4 on reduced graphene oxide sheets is clearly visible from the electron micrographs. Co_xO_y nanoparticles were observed to be aggregated into larger spherical nanoparticles with diameter of 100-200 nm. On the other hang Mn_3O_4 were observed to grow into nanoparticles of 25-100 nm across with a rich amount of planar smooth surfaces. Finally reduced graphene oxides sheets were observed to be wrinkled and free from any nanoparticles. X-ray photoelectron spectroscopy (XPS) was performed to analyze the surface composition of $MnCo_2O_4$/NGr and NGr to reveal the surface nitrogen contents (**Figure 3**). $MnCo_2O_4$/NGr survey reveals the presence of C,O, N,Co and Mn species. High resolution Co2p shows the peaks $2p_{1/2}$ and $2p_{3/2}$ with peak difference of 14.9 eV. The shoulders to the main peaks can be ascribed to the satellite peaks for cobalt. Similarly Mn2p high resolution XPS reveals the presence of $2p_{1/2}$ and $2p_{3/2}$ peaks at 641.8 eV and 652.3 eV respectively. For nitrogen doped carbons, quantity and type of N doping is crucial for electrocatalytic performance. Surface N contents for $MnCo_2O_4$/NGr were measured to be 6.24%. High resolution N1s spectra revealed the presence of pyrolic, pyridinic and graphitic N-types in $MnCo_2O_4$/NGr (Figure 3d).

Pyrolic-N was observed to be 76.28%, pyridinic-N as 15.22% and graphitic-N was found to be 8.49% of the total N. Survey XPS spectrum of NGr shows the presence of only C,O and N (Figure 3e). The absence of metallic impurities confirms the purity of sample. The % N in NGr was measured to be 8.65 % i.e. about 2.5 % more than the $MnCo_2O_4$/NGr. High resolution N1s spectrum reveals the presence of pyrolic, pyridinic and graphitic N-types (Figure 3f). For NGr, Pyrolic-N was observed to be 71.79%, pyridinic-N as 16.3% and graphitic-N was found to be 11.9% of the total N. Compared to $MnCo_2O_4$/NGr, a higher graphitic, lower pyrolic and almost similar pyridinic content are observed in NGr. (Figure S4 in supporting information)

Catalyst inks for all the samples were made and deposited onto GCE for evaluation of their electrocatalytic performance for ORR in alkaline media. Cyclic Voltammograms (CV) in both N_2 and O_2 saturated 0.1 M KOH were recorded as shown in **Figure 4**. In case of O_2 saturated electrolytes, cathodic peak in the 0.8-0.9 V vs. RHE region is attributed to the reduction of molecular oxygen on the surface of the electrocatalysts. From these CVs, a discernable large ($j = 1.72$ mA.cm^{-2}) and most positive ($E = 0.85$ V vs. RHE) reduction peak for molecular oxygen is observed for $MnCo_2O_4$/NGr compared to the rest, highlighting the superior activity of spinel $MnCo_2O_4$ for ORR in alkaline media. The order of catalytic activity for the catalysts based on CV measurements in O_2 saturated KOH solution is $MnCo_2O_4$/NGr > Co_xO_y/NGr > Mn_3O_4/NGr > NGr. The O_2 reduction peak is absent in N_2 saturated electrolytes as shown by the red dashed lines for each catalyst. Redox couples of both Mn^+/Co^+ are present in the N_2 saturated CV plot of $MnCo_2O_4$/NGr whereas only Co^+ and Mn^+ are observed for the N_2 saturated CV plots of Co_xO_y/NGr and Mn_3O_4/NGr respectively. This electrochemical data is in agreement with the structural characterization information of the aforementioned catalysts which indicates the formation of corresponding oxides without the presence of any impurities. For the Co_xO_y/NGr case, taking into account thermodynamic data provided by literature, faradaic phenomenon observed at lower potentials can be associated with Co^{2+}/Co^{3+} redox

transition whereas the other found at higher potentials is attributed to Co^{3+}/Co^{4+} redox transition.[18] In case of Mn_3O_4/NGr two anodic peaks are related to the oxidation of $Mn(OH)_2$ to Mn_3O_4 and Mn_3O_4 to MnOOH respectively, along with a broad cathodic peak as described in literature.[19] The CV curve for graphene treated with ammonia i.e. 'NGr' was observed to be quasi-rectangular in shape along the current-potential axis, without any redox peaks. This demonstrates absence of any Mn^+/Co^+ ions and excellent capacitance behavior with fast diffusion of electrolyte ions over graphene surface.[20]

The ORR activity of the graphene supported electrocatalysts was further investigated by linear scan voltammetery. LSV plots were obtained in O_2 saturated 0.1 M KOH at different rotation rates of catalyst loaded GCE. **Figure 5**a shows the comparative LSVs of different catalysts at 1600 rpm. The superior electrocatalytic activity of $MnCo_2O_4$/NGr nanoparticles is markedly evident from LSVs. The ORR is kinetically controlled over the surface of $MnCo_2O_4$/NGr in the potential range of 0.9-1.1 V vs. RHE, a mix of kinetic and diffusion controlled in 0.8-0.9 V vs. RHE region and becomes diffusion limited from 0.8V vs. RHE onwards. $MnCo_2O_4$/NGr was observed to have an onset potential 'E_o' of 0.93 V vs. RHE and half wave potential of 0.85 V vs. RHE respectively. The half wave potential, an important ORR parameter which describes the performance of catalyst under load, of $MnCo_2O_4$/NGr was only 30mV more negative compared to commercial Pt/C which confirms the superior activity of $MnCo_2O_4$/NGr. This important parameter was also better compared to other recently reported metal oxide decorated carbon nanomaterials such as tetragonal $CoMn_2O_4$/C, cubic $MnCo_2O_4$/C, cobalt ferrite oxide ($CoFe_2O_4$) nanospheres, Co_3O_4/Co_2MnO_4 nanocomposites, $NiCo_2O_4$ on N-doped graphene and surface tuned Co_3O_4 NPs on graphene.[9, 11, 21] Moreover from the TGA plot (Figure S5 in Supporting Information), $MnCo_2O_4$ loading on nitrogenized graphene oxide was determined to be 52.57 %, which is 15 to 30% lower than similar metal oxides on nitrogen doped reduced graphene electrocatalysts for ORR.[7a, 9-10] The thermo gravimetric analysis also revealed a small weight loss due to hydroxyl species at

lower temperature followed by a large weight lost at 300-450 °C due to burning of carbon which is also manifested by the exothermic peak at the same temperatures in the DSC plot. The large ORR activity accompanied with a lower metal oxide loading endorses the superior catalytic activity of $MnCo_2O_4$/NGr at a lower cost. Apart from having more positive onset and half-wave potentials compared to the rest, $MnCo_2O_4$/NGr was observed to have the largest value of limiting current density i.e. 5.12 $mA.cm^{-2}$. The enhanced activity for oxygen reduction of $MnCo_2O_4$/NGr compared to the rest of the catalysts is in agreement with the CV data which shows the most positive values of potential and largest current density for reduction of molecular oxygen on the surface of $MnCo_2O_4$/NGr. The loading effect/content of $MnCo_2O_4$ on NGr support on the electrocatalytic behavior of the $MnCo_2O_4$/NGr was also examined (Figure S6 in Supporting Information). Both ORR and OER behavior of the $MnCo_2O_4$/NGr composite were sensitive to the relative ratio of $MnCo_2O_4$ to NGr. Either too high as in $MnCo_2O_4$/ 0.5 NGr or too low as in $MnCo_2O_4$/ 2 NGr, ratio of $MnCo_2O_4$ to NGr was found to deteriorate the bifunctional catalytic activity of the $MnCo_2O_4$/NGr composite. On the basis of the optimum $MnCo_2O_4$ to NGr ratio of nearly 1:1 (as measured from TGA), we choose $MnCo_2O_4$/NGr for further RDE and battery performance evaluation, as this composition would offer lowest overpotentials during oxygen reduction on battery discharge and oxygen evolution on battery recharge. Furthermore, in order to ascertain the important function of NGr in the $MnCo_2O_4$/NGr composite, we also performed ORR/OER analysis on the pure $MnCo_2O_4$ as well (Figure 5 a, e and f). Both ORR and OER analysis reveals that without the NGr support, pure $MnCo_2O_4$ exhibits poor electrocatalytic activity (Figure S6 in Supporting Information). This is especially significant for ORR in which very negative onset and half wave potentials of 0.7 and 0.6 V vs. RHE respectively, are observed. The reason behind this is the poor electrical conductivity and weak oxygen binding/activating ability of pure metal oxide.[22] The order of activity in terms of half wave potential follows the pattern observed in the CV plots i.e. $MnCo_2O_4$/NGr > Co_xO_y/ NGr > Mn_3O_4/NGr > NGr > pure

$MnCo_2O_4$. A summary of the electrocatalytic parameters of nanocatalysts is provided as Table S1 in supporting information.

ORR on the surface of electrocatalyst is possible by either an inefficient 2 or by more efficient 4 electron transfer pathway. To ascertain the pathway of ORR on the surface of $MnCo_2O_4$/NGr analysis was performed by recording the LSVs at different rotation rates and later plotting i/j against $1/\omega^{1/2}$ (Figure 5b and 5c). The selectivity of $4e^-$ or $2e^-$ pathway is estimated via Koutecky- Levich Equation.

$$1/j = 1/j_k + 1/j_L \quad (1)$$

Where j_k is the kinetic current density and j_L is the diffusion limiting current density.

Also

$$j_k = nFkC_o \quad (2)$$

And

$$j_L = 0.2nFC_oD_o^{2/3}v^{-1/6}\omega^{1/2} \quad (3)$$

Here ω is the angular velocity in rpm, n is transferred electron number, F is the Faraday constant 96485 C/mol, C_o is the bulk concentration of O_2 1.15×10^{-3} mol/L, D_o is the diffusion coefficient of O_2 in electrolyte 1.9×10^{-5} cm^2/s, ν is the kinematic viscosity of the electrolyte 1.1×10^{-2} cm^2/s and k is the electron-transfer rate constant. The linearity and parallelism of the koutecky–Levich slopes at different potentials (0.2-0.5 V vs. RHE) manifests 1st order reaction kinetics with respect to dissolved oxygen.[23] The slope of the KL plots was further used to obtain the electron transfer number at different potentials. An electron transfer number of about 3.9 over a wide potential window manifest the dominance of 4 electron transfer pathway on the surface of $MnCo_2O_4$/NGr (inset Figure 5c). Comparative results for Co_xO_y/NGr, Mn_3O_4/NGr and NGr revealed electron transfer numbers of 3.61, 3.8 and 3.6 respectively. The mechanism of ORR catalytic activity on the $MnCo_2O_4$/NGr catalyst was further examined from the Tafel slope at low overpotential in O_2-saturated 0.1 M KOH

aqueous solution (Figure 5d). Generally for Pt/C, a Tafel plot i.e. V vs. log j_k shows two distinct slopes at low and high overpotentials, respectively.[24] The two slopes can be described in term of the isotherms at two different oxygen coverages ; 1) at low overpotential the Temkin isotherm, which is associated with high O_2 coverage during ORR and a tafel slope value in the vicinity of 60 mV/dec, governs ORR, whereby the first electron transfer step involving an adsorbed product such as OH^- is the rate determining step ; and 2) at high overpotential the Langmuir isotherm marked with low O_2 coverage and a tafel slope of around 120 mV/dec directs ORR, wherein significant oxide coverage ceases to exist, which is generally the case when a two-electron transfer reaction is the rate-determining step. For Pt/C and $MnCo_2O_4$/NGr, tafel slopes of 85 mV/dec and 80 mV/dec respectively, manifests a temkin isotherm phenomenon to be dominant for ORR.

The ECSA of a catalyst plays a vital role in determining its activity towards ORR. For metal oxides loaded onto graphene, normalizing the double layer capacitance with the specific capacitance is a useful technique to get the ECSA according to Equation 4.[25]

$$ECSA = {}^{C_{DL}}/_{C_s} \quad (4)$$

Non-Faradaic region was first identified and the $MnCo_2O_4$/NGr loaded GCE was cycled at different scan rates in the potential window of 0.1 V in this region. The plot of scan rate vs. current has a linear relation for both anodic and cathodic scans according to Equation 5.

$$i_c = vC_{DL} \quad (5)$$

Where i_c is the capacitive current, v is the scan rate and C_{DL} is the double layer capacitance. The slope of this plot was obtained and average of this slope was the double layer capacitance 'C_{DL}'(Figure S7 in Supporting Information). ECSA was then estimated by normalizing double layer capacitance 'C_{DL}' with the specific capacitance 'C_s'.[25-26] Specific activity of the electrocatalysts at 0.85 V vs. RHE was then determined by dividing the kinetic current with the ECSA as tabulated in Table S1 and Figure S8 in Supporting Information. $MnCo_2O_4$/NGr

was found to have the largest value of SA compared to Co_xO_y/NGr, Mn_3O_4/NGr and NGr. It was about 1.5 times more than that of Co_xO_y/NGr, 8.5 times of Mn_3O_4/NGr and 21 times better than NGr. Moreover the mass activity also followed a similar trend i.e. $MnCo_2O_4$/NGr>Co_xO_y/NGr>Mn_3O_4/NGr >NGr. The superior catalytic activity of $MnCo_2O_4$/NGr compared to the rest can be explained in terms of presence of mix valence of both manganese Mn^{+2}/Mn^{+3} and cobalt Co^{+2}/Co^{+3} in the cubic spinel $MnCo_2O_4$.[10] The introduction of transition metal cations in nitrogen doped carbons lead to the formation of M— N—C bonds which provide these nano-materials high activity and stability in corrosive ORR environment.[27] This finding is also in line with the recent report on Co-N-C moieties to be the active sites for ORR in metal coordinated with nitrogen enriched graphene shells.[28]

Apart from being highly active for ORR in alkaline media, $MnCo_2O_4$/NGr was observed to be extremely active for oxygen evolution reaction as well (Figure 5e). $MnCo_2O_4$/NGr was observed to have the most negative value of onset potential vs. RHE compared to Pt/C, Co_xO_y/NGr, Mn_3O_4/NGr and NGr. Moreover, $MnCo_2O_4$/NGr had the smallest over potential to reach a current density of 10 $mA.cm^{-2}$. An important parameter to gauge the bifunctional ORR/OER activity of an electrocatalyst is the oxygen electrode activity 'ΔE' to reach a current density of 10 $mA.cm^{-2}$ for OER and 3 $mA.cm^{-2}$ for ORR. This value was measured to be 0.91 V for the $MnCo_2O_4$/NGr which is better than a number of similar metal oxides deposited onto graphene. [21a, 21b, 29] The value of ΔE for Co_xO_y/NGr, NGr and Pt/C was found to be 1.04, 1.31 and 1.07 V respectively (Figure 5f). Mn_3O_4 decorated graphene was observed to be a poor OER catalyst as it was unable to achieve a current density of 10 $mA.cm^{-2}$.

Apart from high activity and low cost another desirable feature of ORR electrocatalyst is long term durability in the corrosive alkaline media. For example, Pt/C on carbon is highly active for ORR but it is also highly instable in alkaline media.[6] Over course of time particle agglomeration, coarsening and leaching into the electrolytes have been identified as possible degradation causes for Pt/C. To address this issue, both short term stability (amperometric i-t

test) and long term durability (accelerated durability test ADT) tests were conducted on $MnCo_2O_4$/NGr. The superior stability of $MnCo_2O_4$/NGr and huge instability of Pt/C is clearly evident from the i-t test performed at constant potential of 0.665 V vs. RHE for both catalysts under O_2 saturated alkaline environment (**Figure 6**a). A 22% decrease in the initial value of current was observed for Pt/C over a short period of time which is in agreement with other reports on Pt/C.[21b, 30] On the other hand for $MnCo_2O_4$/NGr a very small loss of 3% in normalized current was noted under the same conditions. This trend was also present in the LSV data recorded before and after the amperometric i-t test (Figure 6b). The reason behind the high stability of the $MnCo_2O_4$/NGr compared to commercial Pt/C can be understood by the presence of coordination of the spinel oxide and N doped sites of the nitrogenized graphene. The incorporation of nitrogen in the graphene host has been reported to provide anchoring sites for the metal oxide NPs forming M—N—C bonds which resist the particle dissolution or growth during the ORR.[10, 29] The long term durability of $MnCo_2O_4$/NGr in alkaline media was further assessed by subjecting it to 1000 potential sweeps from 0.6 to 1 V vs. RHE. The LSVs were recorded in a periodic manner as shown in (Figure 6c). A loss of only 17 mV in half-wave potential after 1000 cycles manifests the excellent durability of the $MnCo_2O_4$/NGr in alkaline media supporting its candidacy as an efficient, active and stable electrocatalyst for ORR in metal-air battery and alkaline fuel cells (Figure 6d).

To translate the superior activity and stability $MnCo_2O_4$/NGr in alkaline condition into an energy conversion device, we employed it as an ORR catalyst in a home built primary Zn-air battery. For comparison commercial Pt/C was also coated on a carbon paper and used in a Zn-air battery. The discharge polarization curves along with power density data for both are provided in **Figure 7**a. It is noteworthy to mention that both the plots were recorded from the battery working in ambient air environment which is a more realistic approach to simulate the real life scenario. Moreover testing the Zn−air battery under ambient static air condition is much more practical than testing it with blowing oxygen or water vapor saturated ideal

conditions because of the fact that both the intrinsic activity and architecture of catalysts are sensitive to oxygen and electrolyte diffusion which contributes to the overall cell performance.[31] The primary Zn-air batteries had an open circuit voltage (OCV) of 1.55 V and 1.50 V respectively for commercial Pt/C and $MnCo_2O_4$/NGr respectively. The behavior of the discharge profiles reveal an activation loss region followed by an ohmic loss region. The activation loss section is associated with potential loss due to the activation barrier that a reactant species must overcome whereas the ohmic loss part shows the loss due to the electrical resistance of the components. Pt/C cathode based battery was observed to have a maximum power density of 94.6 $mW.cm^{-2}$ at a current density of 100 $mA.cm^{-2}$ along with a current density of 85 $mA.cm^{-2}$ at a discharge voltage of 1.0 V. These values are in agreement with the data reported for primary Zn-air battery working in ambient air by other researchers.[32] $MnCo_2O_4$/NGr was observed to have a maximum power density of 87 $mW.cm^{-2}$ at a current density of 100 $mA.cm^{-2}$ along with a current density of 70 $mA.cm^{-2}$ at a discharge voltage of 1.0 V. The close resemblance in polarization plots for primary Zn-air batteries made from Pt/C and $MnCo_2O_4$/NGr are in agreement with their LSV data described earlier. In order to assess the long term galvanostatic discharge behavior of $MnCo_2O_4$/NGr loaded Zn-air battery, we operated the battery at medium to high discharge current densities i.e 20-40 $mA.cm^{-2}$ (Figure 7b). The battery was observed to function with stable voltages of 1.2, 1.15 and 1.1 V for discharge loads of 20, 30 and 40 $mA.cm^{-2}$ respectively, for a prolong period of time. These values are superior than the Zn-air battery made from graphene supported $CoMn_2O_4$ (CMO) nanoparticles, Mn, Co co-substituted Fe_3O_4 nanoparticles on nitrogen doped reduced graphene and NiCo alloy with their mixed oxides on carbon nanotubes (CNT).[29, 33] The slight decrease in cell voltage with current density can be explained by the formation of insulating ZnO with high discharge current as explained elsewhere in literature.[9, 34] The final drop in the voltage was due to the consumption of Zn metal anode over the period of time. $MnCo_2O_4$/NGr loaded Zn-air battery was also observed

to have a high specific capacity with a stable voltage profile (Figure 7c). The capacity for the battery was obtained by normalizing the energy retrieved from the battery 'Ah' with the mass of zinc consumed at different current densities. For the $MnCo_2O_4$/NGr loaded battery a specific capacity of 707 $mAh.g^{-1}_{Zn}$ was observed at a discharge current density of 40 $mA.cm^{-2}$. The capacity of the $MnCo_2O_4$/NGr derived Zn-air battery was better compared to the discharge capacities reported in several similar Zn-air systems and even comparable to the more recently introduced hybrid Ni-Zn hybrid air system.[9, 16, 33a] Most strikingly the $MnCo_2O_4$/NGr loaded Zn-air battery was found to be functioning with the same capacity by only replenishing the consumed Zn anode and electrolyte after each discharge (Figure 7d). By refueling the battery periodically, $MnCo_2O_4$/NGr derived Zn-air battery was observed to function with a stable discharge profile for a time period of more than 24 hrs. This result is in agreement with its high stability and durability data found for the $MnCo_2O_4$/NGr in alkaline environment.

The exceptional ORR and OER activity of $MnCo_2O_4$/NGr was further translated into a rechargeable zinc air battery. The $MnCo_2O_4$/NGr loaded zinc air battery was observed to function with extremely stable charge-discharge profile compared to commercial Pt/C (**Figure 8** a, b). For $MnCo_2O_4$/NGr, small charge discharge potential gap (CD) of 0.64 V at j of 1 $mA.cm^{-2}$ for the 1st cycle compared to 0.72 V for Pt/C demonstrates its superior bifunctional activity. Furthermore CD value for Pt/C was observed to increase with time/cycles demonstrating the poor cyclic performance of Pt/C for rechargeable Zn-air battery. At the end of 100th cycle CD was measured to be 0.87 V for Pt/C. A similar decline in performance for Pt/C have been reported which can be understood by the careful examination of stability/durability data.[12, 33a] Possible causes have been identified as oxidation of support, particle agglomeration and dissolution in highly alkaline electrolyte.[6] This leads to higher charge voltage and lower discharge voltage with continuous operation accompanied with the increase of CD gap (Figure 8 a, b). Contrary to this, $MnCo_2O_4$/NGr was observed to function

with extremely stable charge-discharge profile. The CD gap of 0.63 V after 100 cycles validates the superior activity and stability of $MnCo_2O_4$/NGr for rechargeable zinc air system. Furthermore the round-trip efficiency changed by only 0.3% after 100 cycles from initial value of 65.8% to final value of 66.1%. The superior performance of $MnCo_2O_4$/NGr rechargeable Zn-air battery is justified by its electrochemical and durability test data which confirms the stable and good ORR/OER performance in alkaline media compared to commercial Pt/C.

A close examination of the charge-discharge behavior reveals a distinct phenomenon compared to conventional step-cyclic behavior as in Pt/C. Unlike a single plateau charge/discharge profile for OER/ORR, humps in charge-discharge cycle was observed indicating presence of supercapacitive behaviour in $MnCo_2O_4$/NGr rechargeable Zn-air battery (Figure 8c). The charging cycle reveals a distinct hump at 1.75 V over $MnCo_2O_4$/NGr surface followed by the plateau for OER. A similar hump during discharge cycle was also found for $MnCo_2O_4$/NGr. This is in contrast to commercial Pt/C for which a single plateau for OER was observed over the charging cycle (Figure 8d). The deviation of the charge-discharge behavior in $MnCo_2O_4$/NGr compared to commercial Pt/C can be understood by the occurrence of metal oxide oxidation-reduction along with ORR/OER. A similar charge-discharge phenomenon is also reported for nickel cobalt oxide supported on carbon coated nickel foam $NiCo_2O_4$/NiF@C.[15] This transition of metal oxide to hydroxide during charging and conversion to oxide from hydroxide during discharge was observed to improve the charge-discharge cyclic efficiency 'η' measured as the ratio of energy delivered on discharge to energy consumed on charge. For the 5^{th} cycle, $MnCo_2O_4$/NGr Zn-air battery consumed 0.43 Wh for charging and delivered 0.36 Wh on discharge with η of 83.7% (Figure S9 in Supporting Information). Compared to this, Pt/C consumed more Wh during charging and delivered less on discharge for the same cycle thus resulting in a lower cyclic efficiency of 63.9%. More interestingly with the passage of time/cycles, η was observed to deteriorate for

Pt/C. η values of 61.2 and 58.9 measured for 20th and 40th charge-discharge cycle respectively confirms the instability of Pt/C for rechargeable zinc-air battery. η values of 86 and 86.5 % for the 20th and 40th charge-discharge cycles in case of $MnCo_2O_4$/NGr derived zinc battery confirms its superior bifunctional activity and stability. The redox transitions M-O↔M-O-OH can induce hybrid behavior in in $MnCo_2O_4$/NGr derived zinc-air battery. These transitions cause lower energy consumption i.e Wh on charge and renders more Wh during the discharge cycle compared to conventional Zn-air battery (Figure 8e). Apart from better cyclic efficiency, $MnCo_2O_4$/NGr hybrid battery operates at a higher voltage and delivers larger power density during each cycle (Figure 8f). Moreover this charge-discharge behavior is also evident at higher current densities of 5 and 10 mA.cm^{-2} (Figure S10 in Supporting Information). $MnCo_2O_4$/NGr hybrid battery was observed to function with a stable profile for over 150 cycles with a low charge discharge gap of 0.81 V and cyclic efficiency of 75%. More importantly the cyclic efficiency was also stable over the 150 cycles for hybrid $MnCo_2O_4$/NGr battery. The charge discharge gap for $MnCo_2O_4$/NGr hybrid battery is lower by 0.2 V at the same current density compared to recently reported $NiCo_2O_4$/NiF@C hybrid battery. Pt/C on the other hand was observed to be highly instable as observed by increasing charge discharge gap with cycles. Again at higher current density, $MnCo_2O_4$/NGr battery was able to deliver higher power density during discharging as shown in Figure S10d in Supporting Information. This can be associated with the supercapacitive properties of $MnCo_2O_4$/NGr which allow it to work at higher voltage and as such provide high power density and high energy density.

In order to investigate the reason behind the excellent cyclic efficiency and high power density of $MnCo_2O_4$/NGr, we also analyzed its supercapacitive behavior and found that in addition to having remarkable ORR/OER activity and stability, $MnCo_2O_4$/NGr was observed to display remarkable super capacitive properties as well. **Figure 9**a shows the current response of $MnCo_2O_4$/NGr coated Ni-foam against different scan speeds. The strong response with scan rates shows the excellent capacitive nature of the $MnCo_2O_4$/NGr. For reference, the

CV of Ni-Foam current collector was also added which shows its negligible response with scan speeds. The specific capacitance at different scan speeds (Figure 9b) was then calculated by Equation (6).

$$C = {\int I \,.\, dt}/{m.\Delta V} \quad (6)$$

Where I is the reduction/oxidation current, dt is time differential, m is the mass of active material and ΔV is the voltage range of reduction/oxidation sweep segment. $MnCo_2O_4$/NGr nanocomposite was observed to display a high specific capacitance of 585 $F.g^{-1}$ at a scan speed of 5 $mV.s^{-1}$ based on the total sample mass. Even at a very high scan rate of 50 $mV.s^{-1}$, specific capacitance of 314 $F.g^{-1}$ was recorded for $MnCo_2O_4$/NGr. These values are comparable/superior to a number of similar metal oxides on graphene composites reported by different processing routes.[35] Apart from CV, charge-discharge analysis at different current densities also confirmed the excellent super capacitive nature of $MnCo_2O_4$/NGr (Figure 9c). $MnCo_2O_4$/NGr showed high specific capacitance of 591.2 $F.g^{-1}$ at charge-discharge current density of 1 $A.g^{-1}$. In order to confirm the durability, $MnCo_2O_4$/NGr loaded Ni-Foam was cycled for 1000 times at a high charge-discharge current density of 5 $A.g^{-1}$ (Figure 9d). Figure S11a in Supporting Information displays the CV curves before and after 1000 cycles at 5 $A.g^{-1}$. From Equation 6, the specific capacitance was estimated to be 295 $F.g^{-1}$ at 50 mV/s which shows a small decrease i.e. 6% compared to the initial value of 314 $F.g^{-1}$. Ragone Plot (power density vs. energy density) demonstrates the excellent energy storage capability of $MnCo_2O_4$/NGr (Figure S11b in Supporting Information). A high power density of 5 kW/kg^{-1} along with good energy density of almost 20 $Wh.kg^{-1}$confirms the suitability of the $MnCo_2O_4$/NGr to be used for energy storage and conversion applications. The supercapacitive nature of $MnCo_2O_4$/NGr along with its inherent ORR/OER catalytic ability allows the hybrid battery to operate at higher working voltage, high power density and excellent cyclic efficiency compared to conventional Zn-air battery.

3. Conclusion

To conclude, we report a simple and facile hydrothermal route for the synthesis of non-noble metal oxide nanoparticles on graphene. The uniform dispersion of cubic spinel $MnCo_2O_4$ was confirmed by SEM and TEM. The combined mix valence of $Mn^{+2/+3}$ and $Co^{+2/+3}$ in $MnCo_2O_4$ provides higher catalytic activity to $MnCo_2O_4$ for ORR compared to individual cobalt or manganese oxides. Apart from high activity, $MnCo_2O_4$/NGr was observed to be highly stable and durable in alkaline environment. We demonstrated the application of $MnCo_2O_4$/NGr as a cathode catalyst for a primary Zn-air battery working under realistic ambient conditions. The discharge profile of $MnCo_2O_4$/NGr derived Zn-air system was observed to be comparable to the commercial Pt/C along with a high discharge capacity of 787 $mAh.g^{-1}_{Zn}$ at a current density of 20 $mA.cm^{-2}$. The $MnCo_2O_4$/NGr catalyzed mechanical rechargeable Zn-air battery was observed to be refueled and function regularly with no loss in performance which is in agreement with its stability data. Additionally, the $MnCo_2O_4$/NGr was observed to display exceptional super capacitive properties with a good discharge capacity of 591.2 $F.g^{-1}$ at discharge current density of 1 $A.g^{-1}$. By synergizing the electrocatalytic and supercapacitive behavior of $MnCo_2O_4$/NGr, we report a highly stable, efficient and high power hybrid zinc-air battery with low charge-discharge potential gap and exceptional cyclic efficiency of 86% over 100 charge-discharge cycles at 1 $mA.cm^{-2}$. In brief, by synergizing the electrocatalytic and supercapacitive nature of electrocatalyst, we demonstrate that highly active, stable and efficient advanced zinc air batteries can be developed.

4. Experimental Section

Chemicals: cobalt (II) acetate tetrahydrate ($Co(CH_3COO).4H_2O$, > 99.5%) %) and potassium hydroxide (KOH) procured from Guangdong chemicals, Manganese acetate tetrahydrate ($Mn(CH_3COO).4H_2O$, > 99%), Ammonia solution (25-27%) and Zinc strips (Zn, 99.99%) from Tianjin Fuchen, Platinum on carbon (Pt/C, 20%) from Johnson Matthey fuel cells,

Nafion ionomer solution (5%) from Dupont and carbon fiber paper (HCP 120) from Hesen Shanghai Electric, Graphene oxide (GO) solution with concentration 5mg/mL from Tanfeng technology Inc. and Ethanol (C_2H_5OH, >99.7%) from Tianjin Fuyu chemicals. All the Electrolyte solutions were prepared with ultra-pure distilled water (18.25 $M\Omega.cm^{-1}$).

Catalyst synthesis: Manganese cobalt oxide ($MnCo_2O_4$) nanoparticles supported on nitrogen doped reduced graphene oxide i.e. $MnCo_2O_4$/NGr was synthesized by hydrothermal method. In brief, 0.222 mM of cobalt acetate and 0.111 mM of manganese acetate were mixed with 27 mL DI for $MnCo_2O_4$/NGr, followed by stirring for 15 minutes at room temperature. To this 13 mL of GO (5mg/mL) was added and the stirring was continued for 2 hrs. At this point, 0.5 mL of 27% NH_3 solution was added to above and the temperature of the bath was raised to 80 ^oC. Stirring was continued for another 24 hrs followed by which the precursor solution was transferred to a Teflon lined SS autoclave. The autoclave was placed at 150 ^oC for 3 hrs in an oven for hydrothermal treatment. After the heat cycle, autoclaves were allowed to cool naturally in the oven. The solid product was then washed several times with DI and collected by centrifugation. Finally, $MnCo_2O_4$ on graphene were collected by freeze drying and designated as $MnCo_2O_4$/NGr. Co_xO_y/NGr and Mn_3O_4/NGr were also made by the same process by simply using only 0.333 mM of each corresponding salt. NGr was made by treating GO with 0.5 mL of 27% NH_3 solution in the same way without using any metallic salt.

Physical characterization: The crystal structure of the catalysts was characterized by using X-ray diffraction (XRD) with Cu Ka radiation on PANalytical X'Pert Pro MPD. The working potential and current employed were 40 KV and 40 mA, respectively. The morphological and structural features of nanocatalysts were observed via field emission scanning electron microscopy (SEM, FEI NovaSEM 450) and high-resolution transmission electron microscopy (HRTEM, FEI Tecnai F30) at 200 kV. DSC/TGA analysis was done in

an oxygen environment by heating at a temperature ramp of 10 °C/min from room temperature to 800 ºC on NETZSCH STA 449 F3 thermal analyzer.

Electrochemical characterization: All electrochemical measurements were carried out on a classic three electrode set-up. The Hg/HgO (1 M KOH, 0.098V vs. SHE) was used as a reference electrode, Pt wire was used as a counter electrode and the working electrode was fabricated by depositing catalyst inks onto a rotating glass carbon electrode (GCE) with a diameter of 5mm. CHI660C electrochemical workstation was used to measure the catalytic activity of catalysts. Cyclic voltammetry (CV) was done in both N_2 and O_2 saturated 0.1 M KOH. Prior to recording of data, N_2 or O_2 was bubbled through the electrolyte for at least 15 minutes. Catalyst ink for CVs and LSVs was made by adding 4 mgs of catalyst to a mixture of ½ mL of ethanol, ½ mL of DI and 10 µL of 5% Nafion ionomer solution. The ink was subjected to sonication for 30 mins and later 5µL of this ink was drop cast onto GCE and air dried for 10 minutes followed by heating in oven for 5 minutes at 50 ºC. The catalyst loading on GCE was estimated to be 0.1 mg.cm^{-2}. Linear Scan Voltammetry (LSV) was performed on the thin film of catalyst nanoparticles deposited on GCE at room temperature in 0.1 M KOH (O_2 saturated). The experiments were performed at a scanning rate of 10 mV.s^{-1} with the rotation rates of 900, 1600, 2500 and 3200 rpm. The measured current was normalized to the geometric area of the catalyst layer on GCE and the potentials were converted to reversible hydrogen electrode (RHE) scale according to Nernst equation; $E_{RHE}= E_{Hg/HgO}+0.098+0.059*pH$.

Zinc-air battery: Zn-air batteries were made according to a home designed cell configuration. For primary and mechanically rechargeable Zn-air battery; catalyst ink was made by adding 4 mgs of catalyst powder with 2 mgs of Vulcan XC-72 followed by dispersion in a solution of 1 mL ethanol and 40 µL 5% nafion ionomer. After sonication for 30 mins, this ink was drop casted onto hydrophobic carbon paper to get a catalyst loading of 1.2 mg.cm^{-2}. The carbon paper was later dried for 30 mins at 70 ºC and later coupled with a zinc foil through 6 M KOH

to form a Zn-air cell. Porous glass membrane was used as a separator between anode and air-cathode. For rechargeable $MnCo_2O_4$/NGr derived zinc air battery, nickel foam was first cleaned with dilute sulfuric acid for 15 min and soaked in acetone solution for 2 hours. The nickel foam current collector was then washed with deionized water and dried in oven at 70 ^oC for 2 hrs. The cleaned nickel foam was finally placed into the Teflon lined autoclave for direct hydrothermal deposition of $MnCo_2O_4$/NGr. After hydrothermal treatment, nickel foam was washed several times with DI to remove loose particles. Subsequently $MnCo_2O_4$/NGr deposited nickel foam was dried at 70 ^oC for 2 hrs. Gas diffusion layer (GDL) was made by mixing 0.5 g of acetylene black, 2.5 ml of PTFE (65%) and 15 ml of absolute ethanol with 5 ml of deionized water and stirring was done for 3 hours to form a colloidal solution. This colloidal solution was separated in an ultrasonic bath for 15 minutes and bath was heated at 80 ^oC water for 10 minutes to get the acetylene black colloid. The gas diffusion layer (0.5 mm thick) was obtained by drying this colloid and pressing at 10 MPa pressure for 30 min. To prepare the air electrode, $MnCo_2O_4$/NGr loaded nickel foam and GDL were rolled to a thickness of 0.5 mm and dried for 30 min at 70 ^oC. The air electrode was coupled to zinc strip anode via 6 M KOH + 0.2 M zinc acetate electrolyte in a home built cell. The performance of the zinc-air batteries was measured and recorded through a battery testing system CT 2001A (LANHE Company) in ambient atmosphere. Battery testing and cycling experiments were performed at 25 ^oC and 1 atmosphere.

Preparation of working electrodes: The working electrode for supercapacitor test was prepared by mixing $MnCo_2O_4$/NGr, Acetylene black and Polytetrafluoroethylene (60 wt%) with a mass ratio of 80:10:10. $MnCo_2O_4$/NGr and Acetylene black were first ground and added to DI to form slurry to which PTFE was subsequently added. The ink was then coated onto nickel foam which was used as a current collector and pressed at 10 MPa followed by drying overnight at 70 ºC. All electrochemical experiments were carried out in 6 $mol \cdot L^{-1}$ KOH using a three-electrode system, in which platinum wire and Hg/HgO electrodes were used as counter and reference electrodes, respectively. Cyclic voltammetry (CV) tests and galvanostatic charge-discharge measurements were performed on a CHI660C electrochemical workstation. Cyclic stability was performed by 1000 charge-discharge cycles at 5 $A.g^{-1}$, after which the 6M KOH was replaced with fresh solution and then CV was recorded at 50 $mV.s^{-1}$.

Supporting Information

Supporting Information is available from the Wiley Online Library or from the author.

Acknowledgements

This study was supported by the National Natural Science Foundation of China (grant nos. 51271148 and 50971100), the Research Fund of State Key Laboratory of Solidification Processing in China (grant no. 150-ZH-2016), the Aeronautic Science Foundation Program of China (grant no. 2012ZF53073), the Science and Technology Innovation Fund of Western Metal Materials (grant no. XBCL-2-11) and the Doctoral Fund of Ministry of Education of China (grant no. 20136102110013).

Received: ((will be filled in by the editorial staff))
Revised: ((will be filled in by the editorial staff))
Published online: ((will be filled in by the editorial staff))

References

[1] Y. Huang, M. Zhu, Y. Huang, Z. Pei, H. Li, Z. Wang, Q. Xue, C. Zhi, Advanced Materials **2016**, 28, 8344.
[2] a)S. T. K. Jang-Soo Lee, Advanced Energy Materials **2011**, 1, 34; b)M. A. Rahman, X. J. Wang, C. Wen, Journal of Applied Electrochemistry **2014**, 44, 5; c)S. H. C. Xiongwen Zhang, international journal of hydrogen energy **2015**, 40, 6866.
[3] a)A. Kraytsberg, Y. Ein-Eli, Journal of Power Sources **2011**, 196, 886; b)A. K. a. Y. E.-E. Moran Balaish, Phys.Chem.Chem.Phys **2014**, 16, 2801.

[4] J.-S. Lee, S. Tai Kim, R. Cao, N.-S. Choi, M. Liu, K. T. Lee, J. Cho, Advanced Energy Materials **2011**, 1, 34.
[5] a)F. R. McLarnon, E. J. Cairns, Journal of The Electrochemical Society **1991**, 138, 645; b)P. Pei, K. Wang, Z. Ma, Applied Energy **2014**, 128, 315; c)V. Caramia, B. Bozzini, Materials for Renewable and Sustainable Energy **2014**, 3, 28.
[6] A. Zadick, L. Dubau, N. Sergent, G. Berthome, M. Chatenet, Acs Catalysis **2015**, 5, 4819.
[7] a)Y. Y. Liang, Y. G. Li, H. L. Wang, J. G. Zhou, J. Wang, T. Regier, H. J. Dai, Nature Materials **2011**, 10, 780; b)R. Ning, J. Q. Tian, A. M. Asiri, A. H. Qusti, A. O. Al-Youbi, X. P. Sun, Langmuir **2013**, 29, 13146; c)Z. Q. Liu, Q. Z. Xu, J. Y. Wang, N. Li, S. H. Guo, Y. Z. Su, H. J. Wang, J. H. Zhang, S. Chen, International Journal of Hydrogen Energy **2013**, 38, 6657.
[8] a)M. Sun, H. Liu, Y. Liu, J. Qu, J. Li, Nanoscale **2015**, 7, 1250; b)Q. Liu, Z.-F. Li, Y. Liu, H. Zhang, Y. Ren, C.-J. Sun, W. Lu, Y. Zhou, L. Stanciu, E. A. Stach, J. Xie, Nature Communications **2015**, 6, 6127; c)B. Xia, Y. Yan, X. Wang, X. W. Lou, Materials Horizons **2014**, 1, 379.
[9] S. K. Singh, V. M. Dhavale, S. Kurungot, Acs Appl Mater Inter **2015**, 7, 21138.
[10] Y. Y. Liang, H. L. Wang, J. G. Zhou, Y. G. Li, J. Wang, T. Regier, H. J. Dai, J Am Chem Soc **2012**, 134, 3517.
[11] P. W. Menezes, A. Indra, N. R. Sahraie, A. Bergmann, P. Strasser, M. Driess, ChemSusChem **2015**, 8, 164.
[12] M. Prabu, P. Ramakrishnan, S. Shanmugam, Electrochemistry Communications **2014**, 41, 59.
[13] G. Zhang, B. Y. Xia, X. Wang, X. W. Lou, Advanced Materials **2014**, 26, 2408.
[14] a)Z. K. Yang, Z.-W. Zhao, K. Liang, X. Zhou, C.-C. Shen, Y.-N. Liu, X. Wang, A.-W. Xu, Journal of Materials Chemistry A **2016**, 4, 19037; b)H. Hu, L. Han, M. Yu, Z. Wang, X. W. Lou, Energy & Environmental Science **2016**, 9, 107.
[15] B. Li, J. Quan, A. Loh, J. Chai, Y. Chen, C. Tan, X. Ge, T. S. A. Hor, Z. Liu, H. Zhang, Y. Zong, Nano Letters **2017**, 17, 156.
[16] D. U. Lee, J. Fu, M. G. Park, H. Liu, A. Ghorbani Kashkooli, Z. Chen, Nano Letters **2016**, 16, 1794.
[17] D. Yuming, H. Kun, Y. Lin, Z. Aimin, Nanotechnology **2007**, 18, 435602.
[18] a)H. G. Meier, J. R. Vilche, A. J. Arvía, Journal of Electroanalytical Chemistry and Interfacial Electrochemistry **1982**, 138, 367; b)K. Kumar, C. Canaff, J. Rousseau, S. Arrii-Clacens, T. W. Napporn, A. Habrioux, K. B. Kokoh, The Journal of Physical Chemistry C **2016**, 120, 7949.
[19] a)B. Messaoudi, S. Joiret, M. Keddam, H. Takenouti, Electrochimica Acta **2001**, 46, 2487; b)Y. F. Liu, G. H. Yuan, Z. H. Jiang, Z. P. Yao, Journal of Nanomaterials **2014**, 2014, 11.
[20] a)X. Zhang, D. Zhang, Y. Chen, X. Sun, Y. Ma, Chinese Science Bulletin **2012**; b)K. Sheng, Y. Sun, C. Li, W. Yuan, G. Shi, Scientific Reports **2012**, 2, 247.
[21] a)W. Yan, X. Cao, K. Ke, J. Tian, C. Jin, R. Yang, RSC Advances **2016**, 6, 307; b)D. Wang, X. Chen, D. G. Evans, W. Yang, Nanoscale **2013**, 5, 5312; c)H. Zhang, H. Y. Li, H. Y. Wang, K. J. He, S. Y. Wang, Y. G. Tang, J. J. Chen, Journal of Power Sources **2015**, 280, 640.
[22] C. Li, X. Han, F. Cheng, Y. Hu, C. Chen, J. Chen, Nature Communications **2015**, 6, 7345.
[23] J. Xiao, Q. Kuang, S. Yang, F. Xiao, S. Wang, L. Guo, Scientific Reports **2013**, 3, 2300.
[24] A. Qaseem, F. Chen, X. Wu, R. L. Johnston, Catalysis Science & Technology **2016**.
[25] C. C. L. McCrory, S. Jung, J. C. Peters, T. F. Jaramillo, J Am Chem Soc **2013**, 135, 16977.

[26] a)S. Ghosh, P. Kar, N. Bhandary, S. Basu, S. Sardar, T. Maiyalagan, D. Majumdar, S. K. Bhattacharya, A. Bhaumik, P. Lemmens, S. K. Pal, Catalysis Science & Technology **2016**, 6, 1417; b)S. K. Bikkarolla, P. Cumpson, P. Joseph, P. Papakonstantinou, Faraday Discussions **2014**, 173, 415; c)H. S. Jeon, M. S. Jee, H. Kim, S. J. Ahn, Y. J. Hwang, B. K. Min, Acs Appl Mater Inter **2015**, 7, 24550.
[27] a)Y. Liu, H. Jiang, Y. Zhu, X. Yang, C. Li, Journal of Materials Chemistry A **2016**, 4, 1694; b)Z. Wang, S. Xiao, Z. Zhu, X. Long, X. Zheng, X. Lu, S. Yang, Acs Appl Mater Inter **2015**, 7, 4048.
[28] M. Zeng, Y. Liu, F. Zhao, K. Nie, N. Han, X. Wang, W. Huang, X. Song, J. Zhong, Y. Li, Adv Funct Mater **2016**, 26, 4397.
[29] Y. Zhan, C. Xu, M. Lu, Z. Liu, J. Y. Lee, Journal of Materials Chemistry A **2014**, 2, 16217.
[30] a)Y. Wang, X. Lu, Y. Liu, Y. Deng, Electrochemistry Communications **2013**, 31, 108; b)X. Yan, Y. Jia, J. Chen, Z. Zhu, X. Yao, Advanced Materials **2016**, 28, 8771.
[31] a)Y. Li, M. Gong, Y. Liang, J. Feng, J.-E. Kim, H. Wang, G. Hong, B. Zhang, H. Dai, Nature Communications **2013**, 4, 1805; b)Z. Wang, S. Xiao, Y. An, X. Long, X. Zheng, X. Lu, Y. Tong, S. Yang, Acs Appl Mater Inter **2016**, 8, 13348.
[32] a)X. Wu, F. Chen, N. Zhang, A. Qaseem, R. L. Johnston, Journal of Materials Chemistry A **2016**, 4, 3527; b)G. Nam, J. Park, S. T. Kim, D. B. Shin, N. Park, Y. Kim, J. S. Lee, J. Cho, Nano Letters **2014**, 14, 1870.
[33] a)M. Prabu, P. Ramakrishnan, H. Nara, T. Momma, T. Osaka, S. Shanmugam, Acs Appl Mater Inter **2014**, 6, 16545; b)X. Liu, M. Park, M. G. Kim, S. Gupta, G. Wu, J. Cho, Angewandte Chemie International Edition **2015**, 54, 9654.
[34] S. Siahrostami, V. Tripkovic, K. T. Lundgaard, K. E. Jensen, H. A. Hansen, J. S. Hummelshoj, J. S. G. Myrdal, T. Vegge, J. K. Norskov, J. Rossmeisl, Physical Chemistry Chemical Physics **2013**, 15, 6416.
[35] a)Y. Yuan, B. Huiping, H. Guangyu, Z. Junwu, C. Haiqun, Chemistry Letters **2014**, 43, 83; b)L. Ren, J. Chen, X. Wang, M. Zhi, J. Wu, X. Zhang, RSC Advances **2015**, 5, 30963; c)L. Li, Y. Q. Zhang, X. Y. Liu, S. J. Shi, X. Y. Zhao, H. Zhang, X. Ge, G. F. Cai, C. D. Gu, X. L. Wang, J. P. Tu, Electrochimica Acta **2014**, 116, 467; d)N. Padmanathan, S. Selladurai, Ionics **2014**, 20, 479.

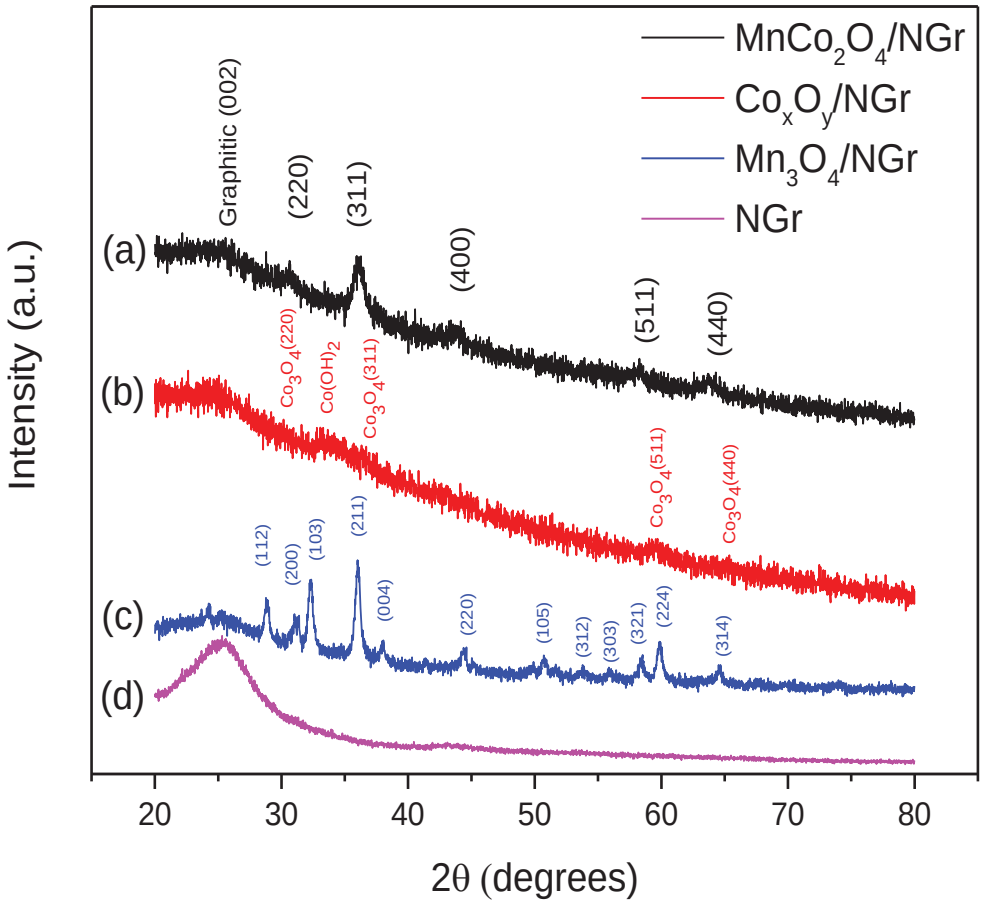

Figure 1 XRD paterns of (a) $MnCo_2O_4$/NGr, (b) Co_xO_y/NGr, (c) Mn_3O_4/NGr and (d) NGr.

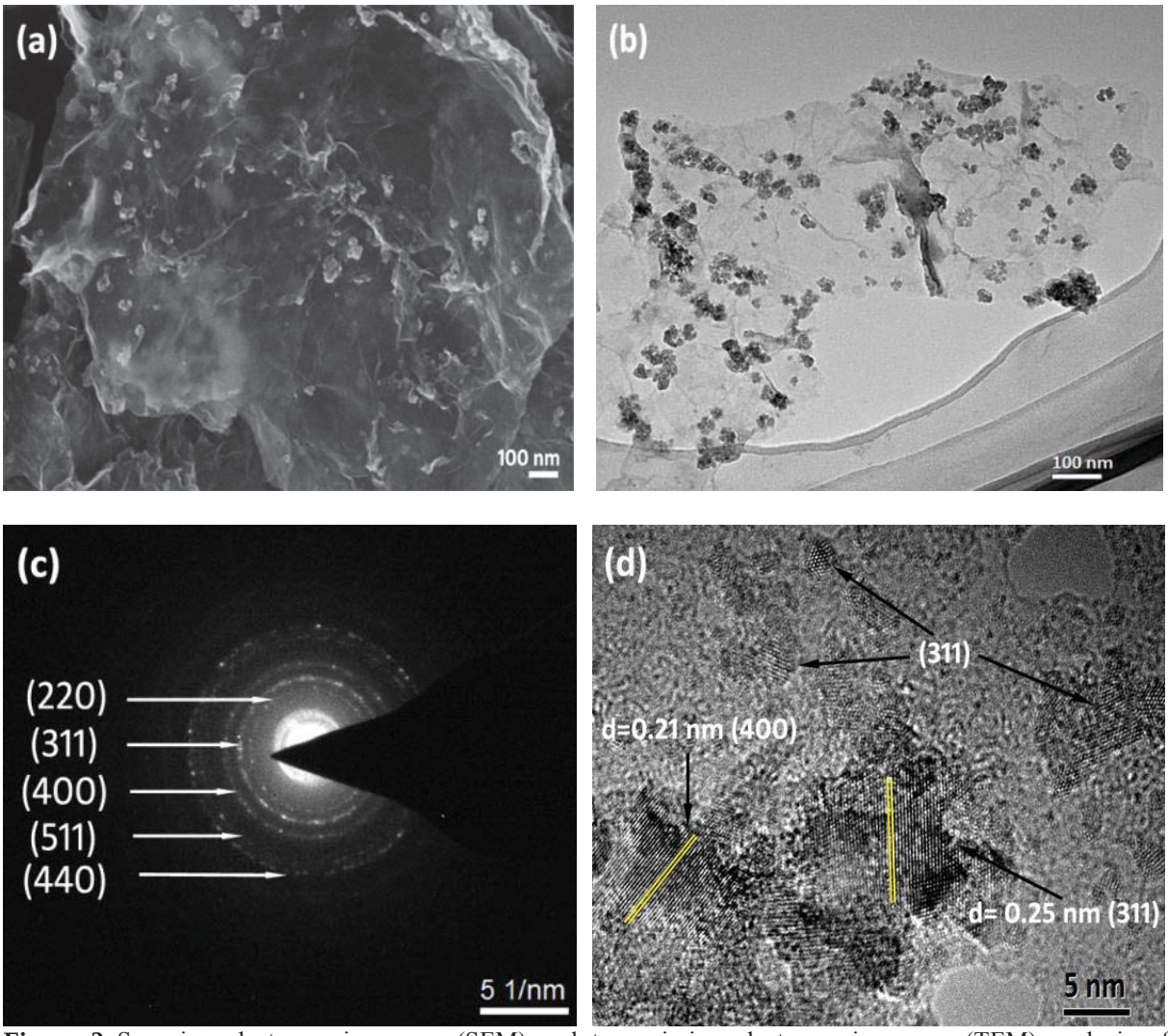

Figure 2 Scanning electron microscopy (SEM) and transmission electron microscopy (TEM) analysis of $MnCo_2O_4$/NGr. (a) Low-magnification SEM image. (b) Low-magnification TEM image. (c) Selected Area Electron diffraction SAED. (d) High-resolution TEM.

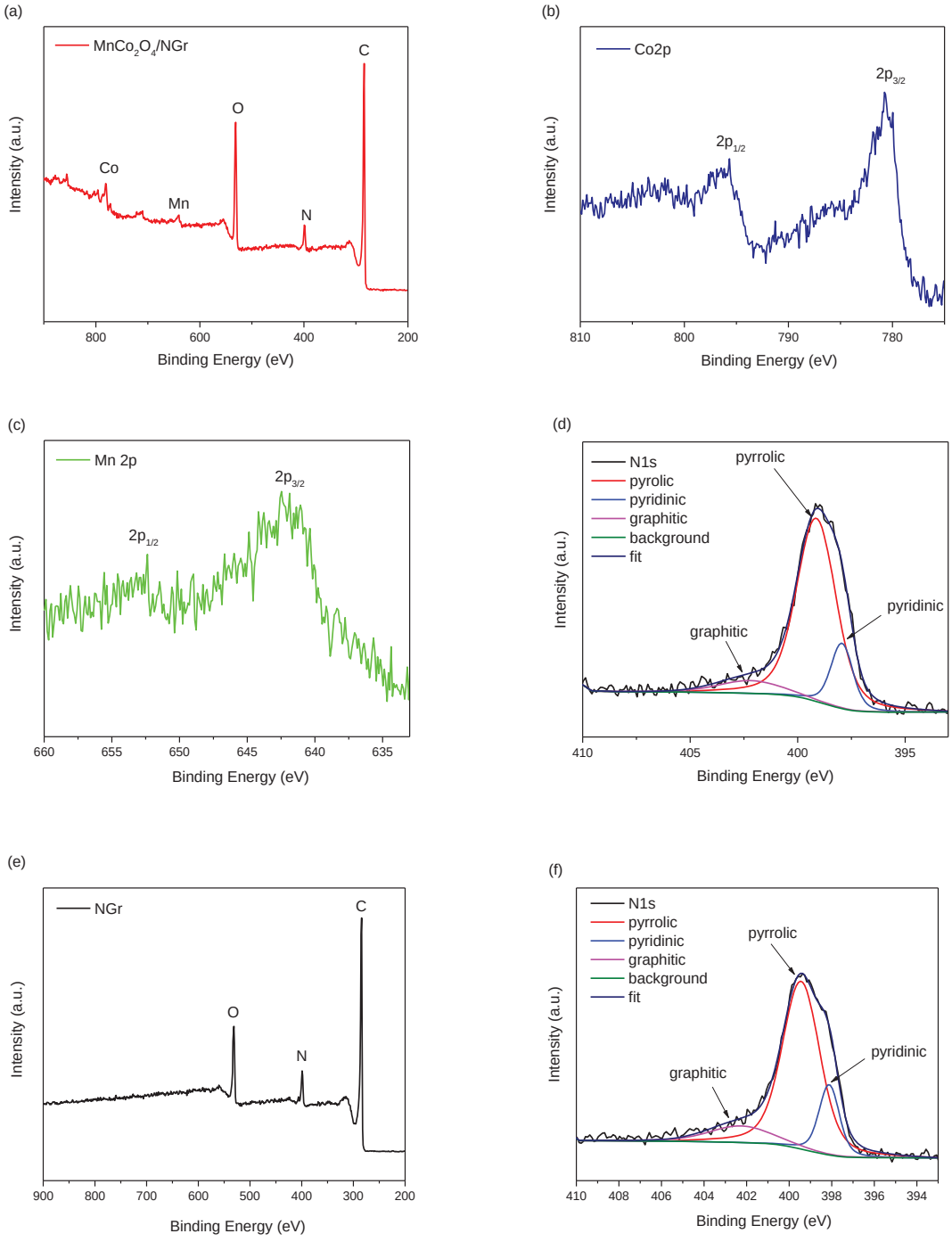

Figure 3 XPS analysis of $MnCo_2O_4$/NGr (a-d) and NGr (e,f). (a) Survey spectra of $MnCo_2O_4$/NGr. (b) High resolution Co2p of $MnCo_2O_4$/NGr. (c) High resolution Mn2p of $MnCo_2O_4$/NGr. (d) High resolution N1s of $MnCo_2O_4$/NGr with peak deconvolution to reveal different N contents. (e) Survey spectra of NGr. (f) High resolution N1s of NGr with peak deconvolution.

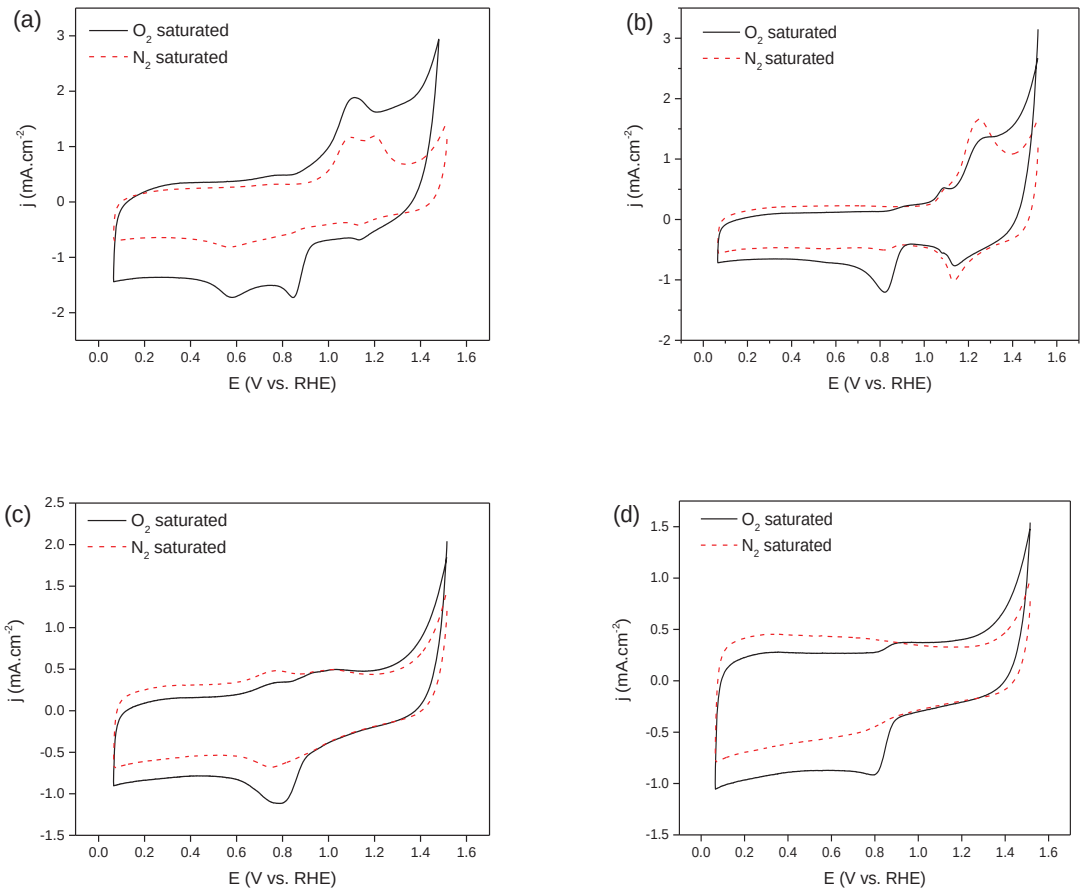

Figure 4 Cyclic voltammetery (CV) of electrocatalysts in O_2 saturated (black solid line) and N_2 saturated (red dashed line) in 0.1 M KOH. (a) $MnCo_2O_4$/NGr , (b) Co_xO_y/NGr, (c) Mn_3O_4/NGr and (d) NGr.

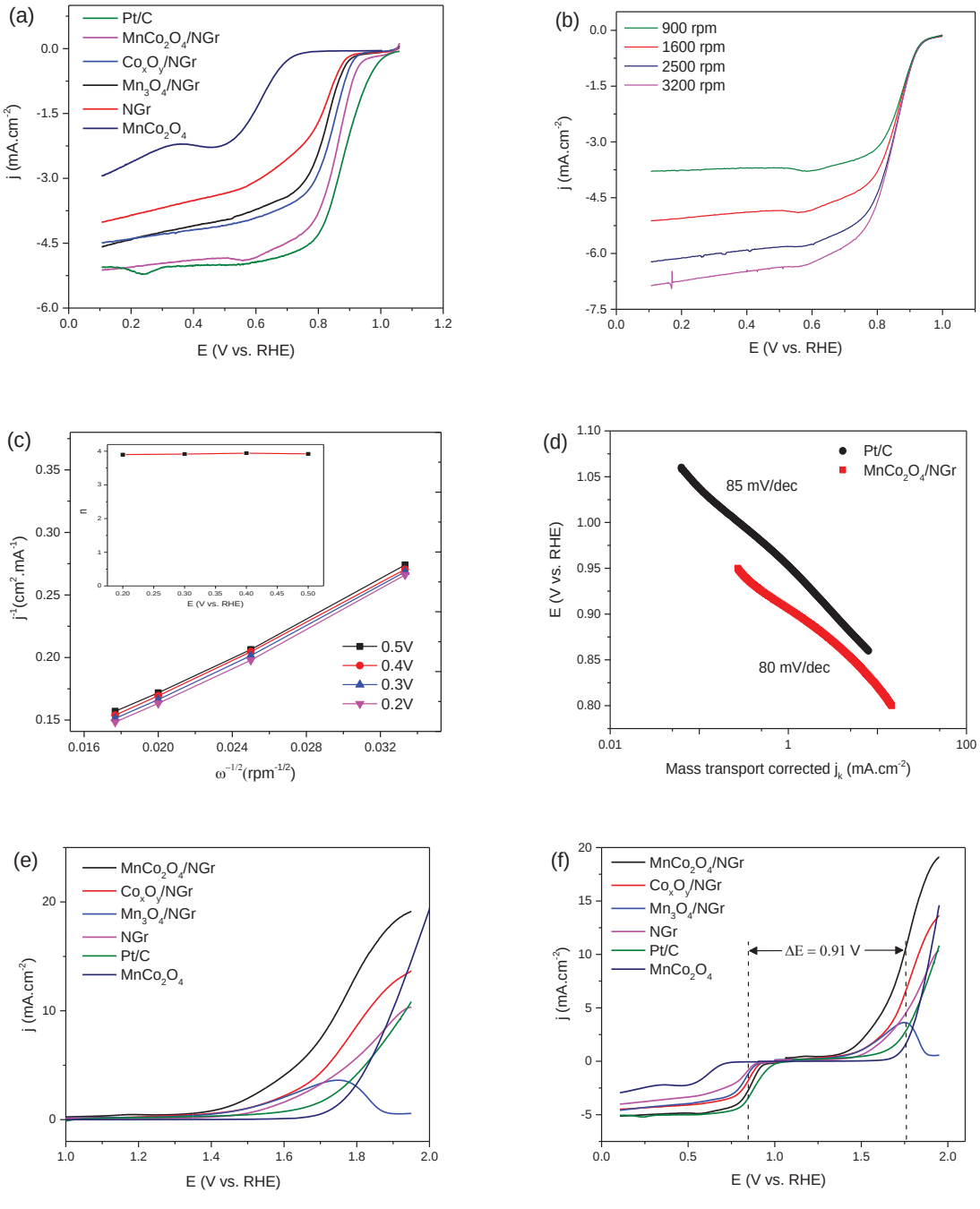

Figure 5 Liner scan voltammetery (LSV) data. (a) LSV of electrocatalysts at 1600 rpm in O_2 saturated 0.1 M KOH, (b) LSV of $MnCo_2O_4$/NGr at 900, 1600, 2500 and 3200 rpm in O_2 saturated 0.1 M KOH, (c) Koutecky-Levich plots of $MnCo_2O_4$/NGr with electron transfer number at different potentials (inset) and (d) Mass transport corrected Tafel plots for $MnCo_2O_4$/NGr and Pt/C. (e) LSV for OER of electrocatalysts at 1600 rpm in O_2 saturated 0.1 M KOH. (f) ORR and OER together to calculate ΔE for electrocatalysts.

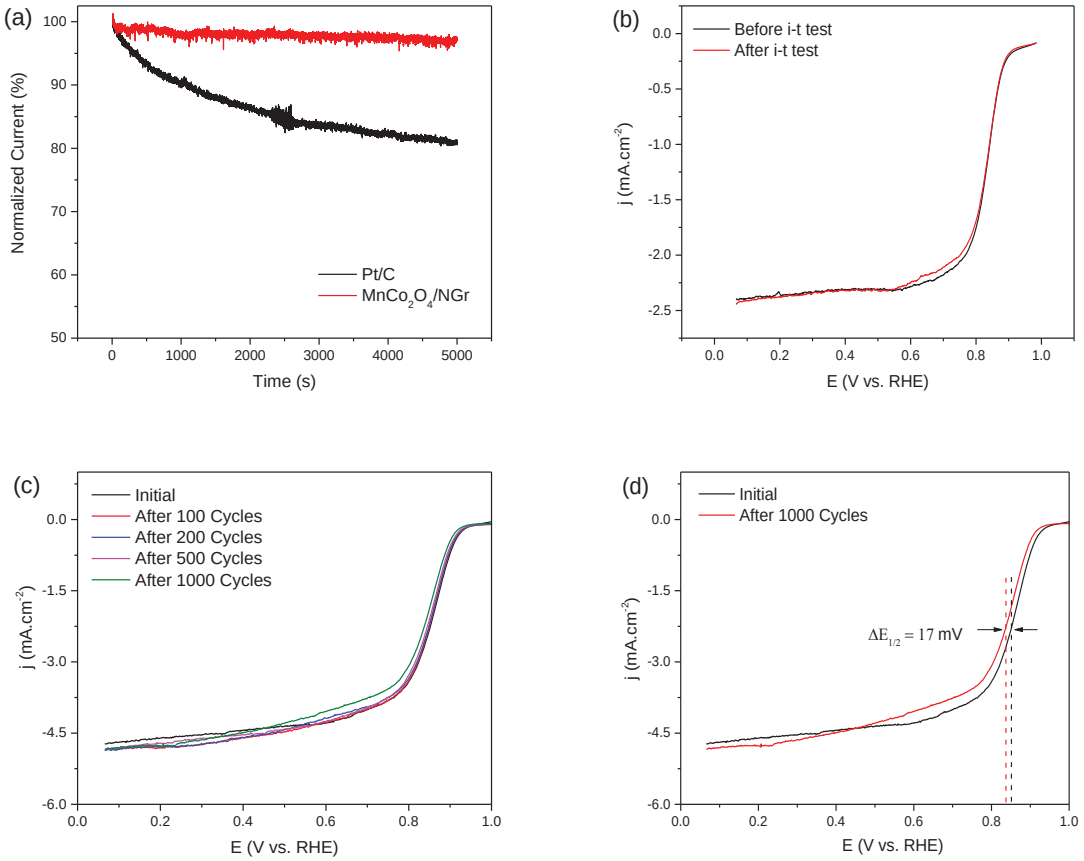

Figure 6 Stability and durability performance. (a) Amperometeric i-t plots for $MnCo_2O_4$/NGr and commercial Pt/C in O_2 saturated 0.1 M KOH at 400 rpm and 0.665 V vs. RHE, (b) LSV comparison before and after i-t test for $MnCo_2O_4$/NGr in O_2 saturated 0.1 M KOH at 400 rpm, (c) Accelerated durability test (ADT) on $MnCo_2O_4$/NGr ; initial LSV and after 100, 200, 500 and 1000 potential cycles. (d) LSV comparison before and after ADT on $MnCo_2O_4$/NGr at 1600 rpm in O_2 saturated 0.1 M KOH.

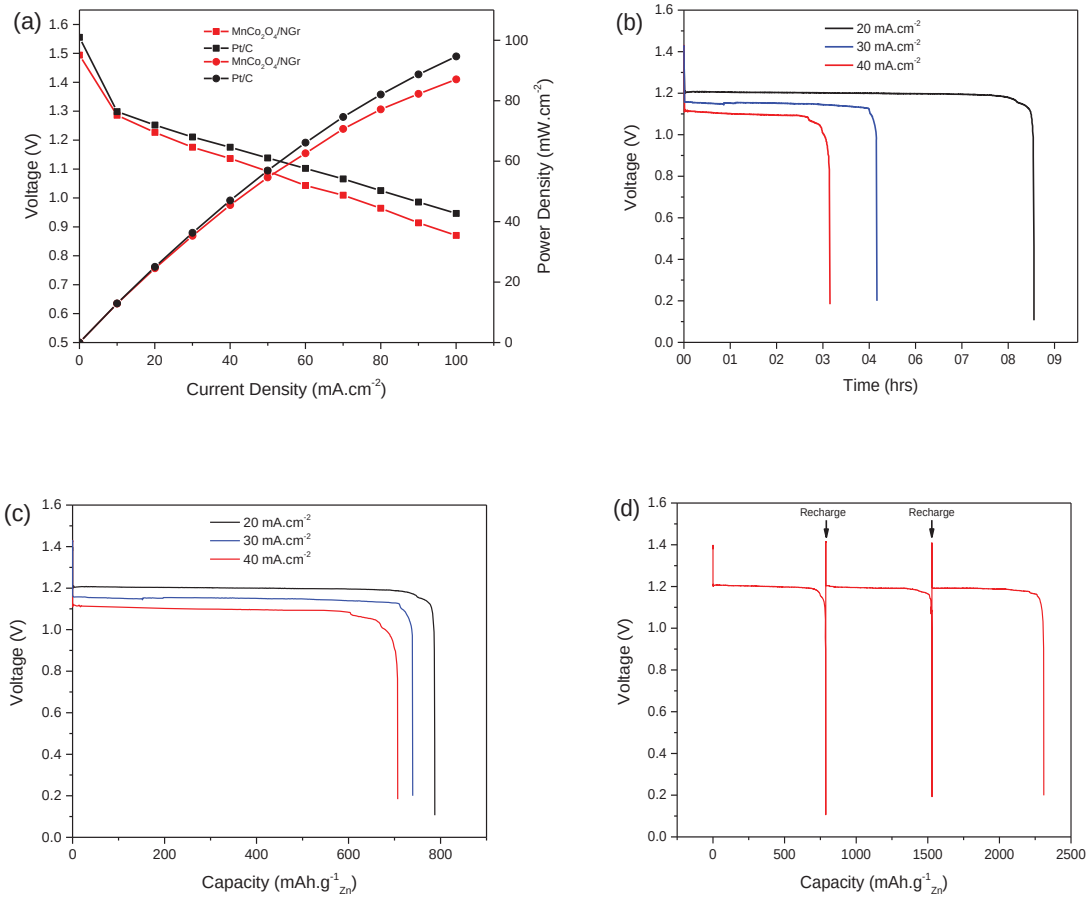

Figure 7 Zinc-air battery performance. (a) Cell voltage and power density polarization curves of a primary zinc-air battery working in ambient air. (b) Discharge profile at current densities of 20, 30 and 40 $mA.cm^{-2}$, respectively. (c) Specific capacity of the zinc-air battery at 20, 30 and 40 $mA.cm^{-2}$, respectively and (d) Mechanical rechargeable Zinc-air battery perfrmance at 20 $mA.cm^{-2}$. The cathode is same $MnCo_2O_4$/NGr while Zn anode and 6M KOH electrolyte are replaced regularly as indicated by the arrows

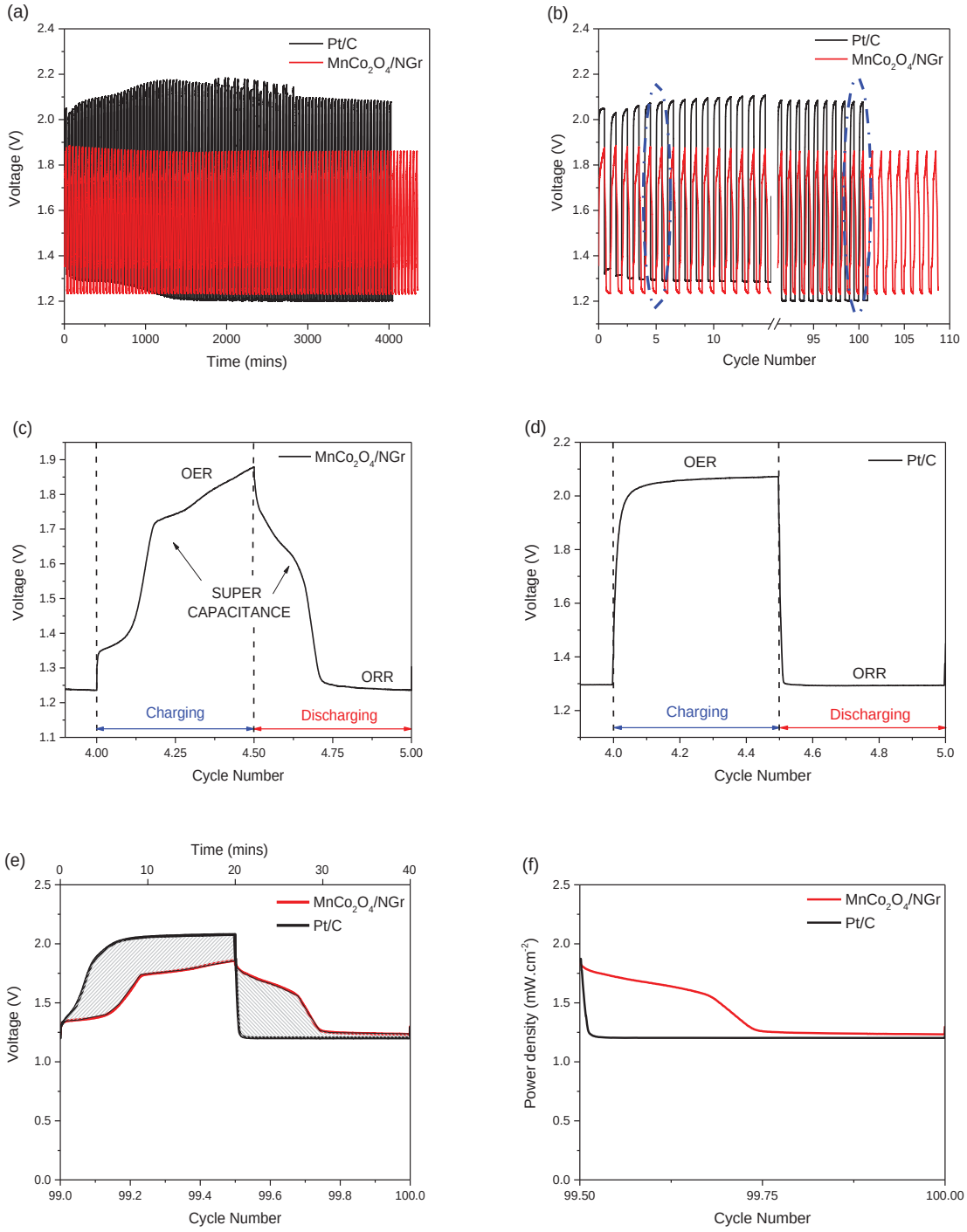

Figure 8 Rechargeable zinc air battery. (a) charge-discharge behavior with time for $MnCo_2O_4$/NGr (red) and Pt/C (black) at 1mA.cm^{-2} with 20 mins charge and 20 mins discharge. (b) overall charge-discharge profile of Zn-air battery for >100 cycles. (c) charge-discharge behavior of $MnCo_2O_4$/NGr at 5th cycle. (d) charge-discharge behavior of Pt/C at 5th cycle. (e) charge-discharge behavior of $MnCo_2O_4$/NGr (red) and Pt/C (black) at 1mA.cm^{-2} for 100th cycle; shaded region shows the less Wh intake during charge and more Wh delivered during discharge by $MnCo_2O_4$/NGr hybrid battery. (f) power density delivered during 100th discharge cycle.

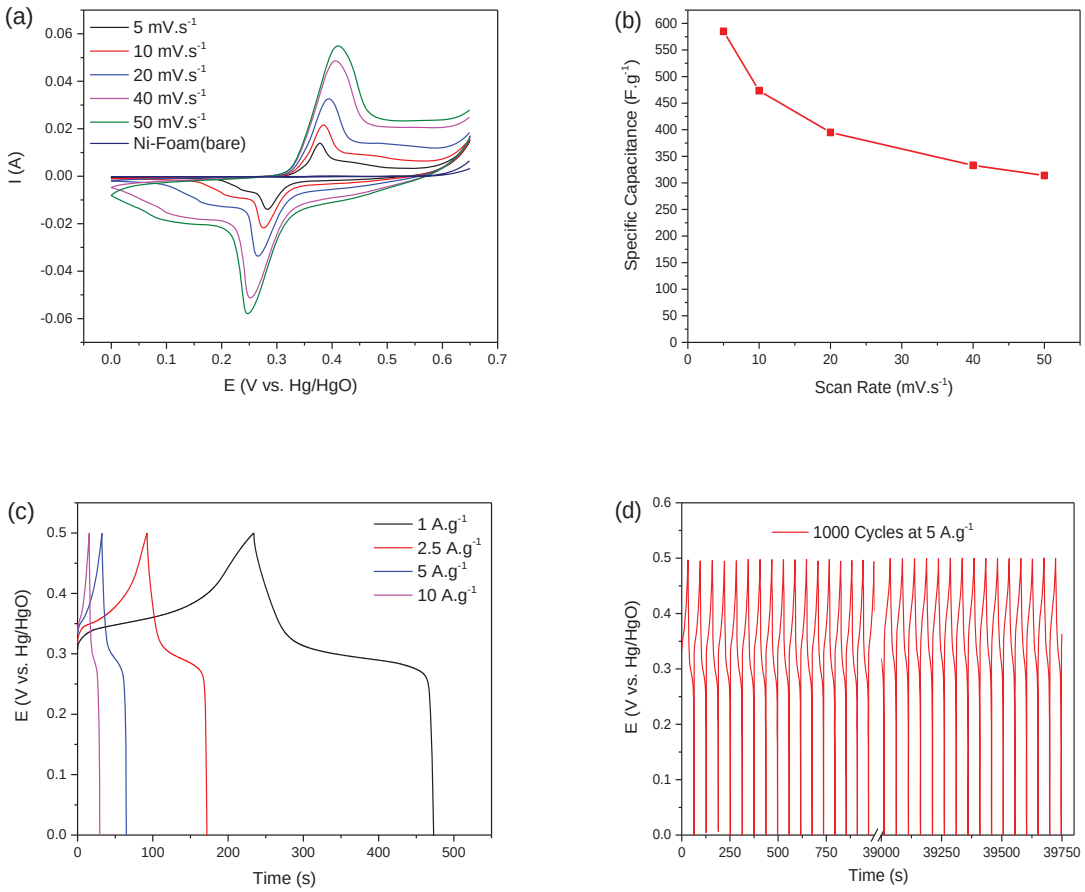

Figure 9 Supercapacitive properties of $MnCo_2O_4$/NGr. (a) CV of $MnCo_2O_4$/NGr loaded on nickel foam at different scan rates in 6M KOH with reference to the bare nickel foam. (b) Specific capacitance of $MnCo_2O_4$/NGr measured at different scan rates. (c) Charge-discharge curves of $MnCo_2O_4$/NGr at current densities of 1, 2.5, 5 and 10 $A.g^{-1}$, respectively. (d) Repeated 1000 charge-discharge cycles at 5 $A.g^{-1}$ on $MnCo_2O_4$/NGr loaded nickel foam.

Manganese cobalt oxide decorated carbon nanomaterial (MnCo$_2$O$_4$/NGr) displays excellent electrocatalytic and supercapacitive behavior. By combining the catalytic and pseudocapacitive characteristics of MnCo$_2$O$_4$, highly stable and efficient rechargeable Zn-air batteries are reported. Hybrid Zn-air battery benefits from this synergistic behavior and works at higher voltage and delivers more power density on discharge with more efficiency compared to conventional Zn-air battery.

bifunctional catalyst, hydrothermal synthesis, primary zinc-air battery, hybrid zinc-air battery, supercapacitor.

Adnan Qaseem , Fuyi Chen*, Chuanzhou Qiu, Abdelaziz Mahmoudi, Xiaoqiang Wu , Xiaolu Wang and Roy L. Johnston*

Manganese Cobalt Oxide Decorated Reduced Graphene Oxide as Multifunctional Material for Mechanically Rechargeable and Hybrid Zinc Air Batteries